NANO LETTERS

Letter

pubs.acs.org/NanoLett

Measuring the Edge Recombination Velocity of Monolayer Semiconductors

Peida Zhao,[†,§] Matin Amani,[†,§] Der-Hsien Lien,[†,§] Geun Ho Ahn,[†,§] Daisuke Kiriya,[†,§] James P. Mastandrea,[‡,§] Joel W. Ager III,[‡,§] Eli Yablonovitch,[†,§] Daryl C. Chrzan,[‡,§] and Ali Javey*[,†,§]

[†]Electrical Engineering and Computer Sciences, [‡]Materials Science and Engineering, University of California at Berkeley, Berkeley, California 94720, United States

[§]Materials Sciences Division, Lawrence Berkeley National Laboratory, Berkeley, California 94720, United States

Supporting Information

ABSTRACT: Understanding edge effects and quantifying their impact on the carrier properties of two-dimensional (2D) semiconductors is an essential step toward utilizing this material for high performance electronic and optoelectronic devices. WS_2 monolayers patterned into disks of varying diameters are used to experimentally explore the influence of edges on the material's optical properties. Carrier lifetime measurements show a decrease in the effective lifetime, $\tau_{effective}$, as a function of decreasing diameter, suggesting that the edges are active sites for carrier recombination. Accordingly, we introduce a metric called edge recombination velocity (ERV) to characterize the impact of 2D material edges on nonradiative carrier recombination. The unpassivated WS_2 monolayer disks yield an ERV $\sim 4 \times 10^4$ cm/s. This work quantifies the nonradiative recombination edge effects in monolayer semiconductors, while simultaneously establishing a practical characterization approach that can be used to experimentally explore edge passivation methods for 2D materials.

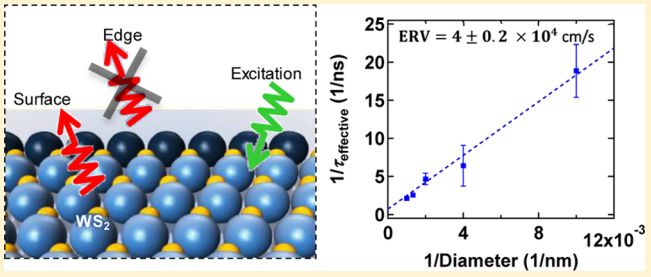

KEYWORDS: *Transition metal dichalcogenide, WS_2, edge recombination velocity, quantum yield, edge effects*

Two-dimensional (2D) semiconductors exhibit unique physical and chemical properties that make them attractive for various electronic and optoelectronic applications.[1−7] Due to their layered structure, 2D material surfaces are inherently self-terminated with well-defined chemical bonds. As a result, their unpassivated surface defect density is dramatically lower than that of most conventional 3D semiconductors. This unique surface property has enabled the observation of near-unity photoluminescence (PL) internal quantum yield (iQY) in large-area monolayer WS_2 and MoS_2 treated with superacids, demonstrating the lack of defect-mediated nonradiative surface recombination.[8−10] However, for most practical device applications, semiconductors need to be etched into proper patterns, often with small areal footprints. While the top and bottom surfaces of 2D semiconductors are chemically self-terminated, their edges can include a high density of dangling bonds that can lead to detrimental effects on carrier properties, especially when the material is patterned into small structures. In this regard, edge effects are important to be quantified and eventually controlled through proper etching and passivation.

Here, we introduce a metric called the edge recombination velocity (ERV) for 2D materials, to quantify the impact of edges on carrier recombination processes. ERV is defined as the total recombination events per unit time at the edge, divided by the product of perimeter length and excess carrier number per unit area. ERV is a direct measure of the tendency for an edge to enhance the recombination rate. Presumably, ERV depends on the detailed structure of the edge in question and can, accordingly, be altered through chemical treatments akin to those used in surface passivation. We note that ERV in a 2D material is analogous to the surface recombination velocity (SRV) used to quantify the surface quality of 3D materials.[11] ERV can be extracted by characterizing the photoluminescence properties of patterned arrays of monolayer disks. We use tungsten disulfide (WS_2) monolayers as a model material system, measuring an ERV of $\sim 4.4 \times 10^4$ cm/s after a chlorine plasma patterning.[12] The ERV value provides a baseline for 2D material edge quality and an assessment platform relevant to any optically active members of the 2D material family.

Figure 1a illustrates the expected light emitting behavior of the WS_2 monolayer disks under optical excitation, where the edge states can induce nonradiative recombination. This edge quenching is associated with the introduction of nonradiative recombination sites during the etching process and the intrinsic metallic nature of certain edge configurations.[13] To quantitatively characterize the radiative quenching, arrays of WS_2 monolayer disks of fixed diameters (d) are fabricated by lithography and dry etching. Subsequently, their PL iQY and

Received: April 27, 2017
Revised: August 10, 2017
Published: August 17, 2017

DOI: 10.1021/acs.nanolett.7b01770
Nano Lett. 2017, 17, 5356−5360

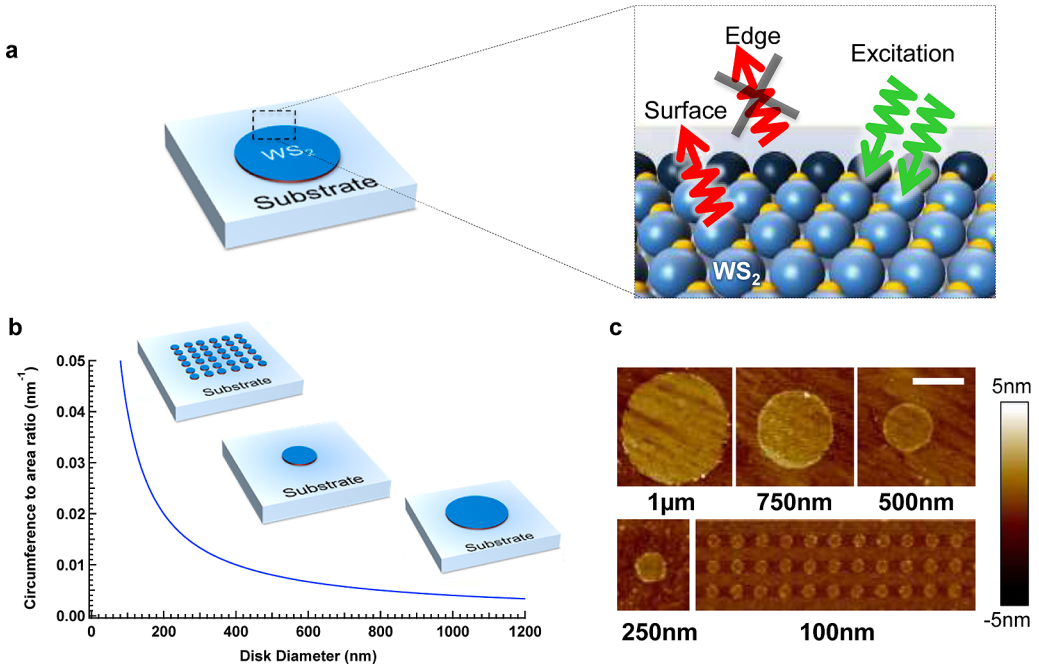

Figure 1. Experimental approach used to probe the WS_2 monolayer edge after a top-down fabrication scheme. (a) Schematic showing optical excitation response. The monolayer only emits at the surface region away from the edge, while the edge itself is expected to recombine the generated carriers nonradiatively. Note that the darker ring at the edge is illustrative only and does not accurately represent the actual atomic structure of the WS_2 edge. (b) Circumference to area ratio of disks fabricated with different diameters, showing a steady increase as diameter decreases (c) Atomic force microscopy (AFM) of WS_2 disks of all chosen diameters. Both the single disks (1 μm to 250 nm) and the array structure (100 nm) are presented. The scale bar is 500 nm for all AFM scans.

effective carrier lifetimes ($\tau_{effective}$) are measured via steady-state and time-resolved PL spectroscopy (TRPL) respectively (see SI for experimental method details).[8] The process is then repeated for different values of d. The circumference to surface area ratio increases as d decreases (Figure 1b). As a result, PL iQY and $\tau_{effective}$ are expected to decrease with decreasing d. Finally, an expression from a diffusion based model (details in the SI) can be used to predict the $\tau_{effective}$ versus d relation. A fit of the experimental data to the theoretical predictions determines the ERV. Figure 1c shows the atomic force microscopy (AFM) images of patterned WS_2 monolayer disks of varying diameters: 1 μm, 750 nm, 500 nm, 250 nm, and 100 nm. Note that, for d = 100 nm, a disk array is adapted to achieve a higher signal-to-noise ratio for photoluminescence measurements.

Figure 2a shows the PL spectra of WS_2 disks ranging from 1 μm to 100 nm in diameter, with the corresponding normalized spectra shown in the inset. The PL spectra are normalized with respect to the fill factor, directly correlating the decreasing intensity trend to an increasingly dominant edge recombination mechanism. Additionally, no obvious subgap emission or peak change is observed across spectra of different diameters shown by the inset, signifying that the radiative recombination mechanism and the optical bandgap remains unaffected for the explored diameter range.[14]

The photoluminescence internal quantum yield (PL iQY) of the WS_2 disks is extracted as a function of pump intensity (corresponding to a calculated exciton generation rate). As shown in Figure 2b, there is a monotonic decrease of iQY as d decreases. The general iQY behavior for larger d disks is consistent with the analytical model proposed in previous studies where a pump-independent and pump-dependent behavior is observed at different generation regimes.[8,10] Specifically, the generated carriers in WS_2 monolayers at steady state, G, can be balanced using a steady state recombination rate, R, via:

$$G = R = B_{nr}n^2 + B_r n^2 \tag{1}$$

where B_{nr} is the nonradiative free carrier recombination rate due to surface defects, n is the free carrier concentration, and B_r is the formation rate of excitons in the system. At the steady state, B_r can be further described via

$$B_r n^2 = \frac{\langle N \rangle}{\tau_{rad}} + C_{bx}\langle N \rangle^2 \tag{2}$$

where $\langle N \rangle$ is the exciton concentration, τ_{rad} is the radiative recombination lifetime, and C_{bx} is the biexcitonic recombination rate.

The above model includes three recombination mechanisms with distinct recombination rates (surface radiative $1/\tau_{rad}$, surface nonradiative B_{nr}, and biexcitonic C_{bx}). The first two mechanisms have the same power dependence and compete directly at the lower generation regime as $R \propto n^2 \propto \langle N \rangle$, while the last mechanism becomes dominant at higher generation regime with $R \propto \langle N \rangle^2$ and contributes to the iQY pump dependence. The model also accurately describes the experimental iQY behavior of an unetched WS_2 monolayer shown in Figure 2b and can be fitted closely utilizing similar values of $1/\tau_{rad}$ and C_{bx} mentioned in our previous work.[10] As d decreases, however, we observe a corresponding iQY decrease at lower generation regime and a convergence of iQY independent of d at the higher generation regime. The clear d dependence at lower pump power points to an edge recombination rate competing with the radiative and surface nonradiative recombination rates. The iQY convergence at higher pump power points to the previously mentioned

DOI: 10.1021/acs.nanolett.7b01770
Nano Lett. 2017, 17, 5356−5360

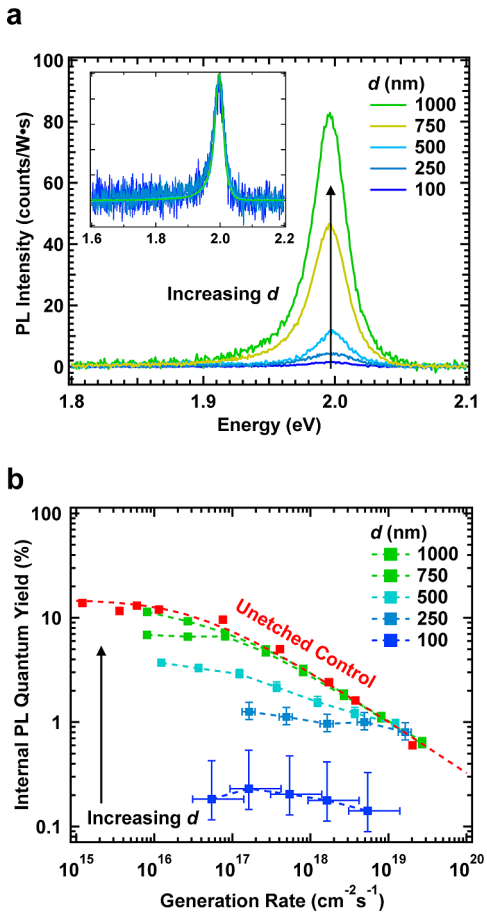

Figure 2. Optical characterizations of WS_2 monolayer disks. (a) Photoluminescence (PL) measurements of WS_2 disks with increasing diameter (corrected for fill factor), showing a steady increase in the emission intensity. The inset shows normalized spectra and indicates that no significant subgap emission is observed across all changing diameters. (b) PL internal quantum yield of WS_2 versus generation rate, as a function of disk diameter. Error bars associated with the samples originate from absorption measurements.

biexcitonic recombination mechanism, overriding the d dependence. As expected, iQY at smaller d seems to exhibit minimal pump dependence, even at the higher generation rates, and is likely due to an increasingly dominant edge recombination competing with the biexcitonic recombination mechanism.

To further understand the edge recombination mechanism and measure ERV, we use TRPL to extract the lifetimes of carriers in WS_2 disks as a function of their diameters. Figure 3 shows the generated exciton concentration decay versus time of different diameter disks, demonstrating a faster lifetime decay as d decreases. As expected, two different regimes of lifetime decay are observed in the TRPL data. At the higher generated exciton density regime, biexcitonic recombination is observed (corresponding to the converging iQY in Figure 2b at the higher generation rate), dominating the lifetime decay across all disk sizes independent of d. As the exciton concentration decays over time, however, lower order recombination mechanisms become observable. These mechanisms can be classified into three types: radiative and nonradiative surface mechanisms, and a nonradiative edge mechanism. To determine the ERV, we fit a decay lifetime $\tau_{effective}$ incorporating all three aforementioned lifetime components at the lower generated exciton density

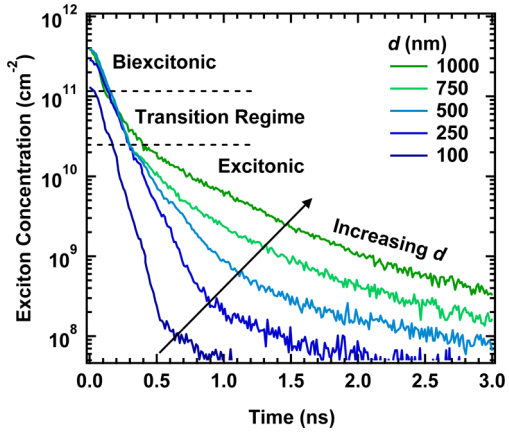

Figure 3. Time-resolved photoluminescence (TRPL) measurements of WS_2 disks. Two distinct decay regimes (with a visible transition) is observed for larger WS_2 disk sizes, while only one regime is seen for smaller sizes. The lifetime extraction is done at the lowest possible generated exciton density where monoexcitonic recombination mechanisms dominate and a clear size dependence is present.

assuming negligible biexcitonic recombinations. In this approximation, a single exponential decay fit can be applied via:[15]

$$\frac{d\langle N\rangle}{dt} = -\frac{\langle N\rangle}{\tau_{effective}} \quad (3)$$

where $\tau_{effective}$ conforms to the following Matthiessen's relation:

$$\frac{1}{\tau_{effective}} = \frac{1}{\tau_{rad}} + \frac{1}{\tau_{nrad}} + \frac{1}{\tau_{edge}} \quad (4)$$

Specifically, τ_{rad} and τ_{nrad} are the surface radiative and nonradiative recombination lifetime measured as 3.4 and 2.4 ns, respectively, in our previous work.[10] Decay curves in Figure 3 are fitted using both a single exponential decay at low generated exciton density as well as convoluting the single exponential decay with a measured instrument response function iteratively against experimental data to ensure accuracy.[16]

Figure 4a plots $1/\tau_{effective}$ vs $1/d$ across multiple disk samples using the previously fitted $\tau_{effective}$ values. The error bars indicate the standard deviation of all measured samples with the same designed d. To find the ERV, we first experimentally determine τ_{rad} and τ_{nrad} from an unetched WS_2 monolayer and collect them under a single time constant $\tau_{surface}$:

$$\tau_{surface} = \left(\frac{1}{\tau_{rad}} + \frac{1}{\tau_{nrad}}\right)^{(-1)} = 1.37 \text{ ns} \quad (5)$$

Subsequently, τ_{edge} is extracted from the measured $\tau_{effective}$ for each disk diameter. Using the diffusion model presented in Supporting Information, τ_{edge} and ERV are related by the following expression:

$$\tau_{edge} = \frac{d}{4 \times \text{ERV}} \quad (6)$$

where ERV has units of length/time.

With eq 6, we fit the experimental $1/\tau_{effective}$ vs $1/d$ curve with a linear slope of (4× ERV) and find an ERV of $\sim 4 \pm 0.2 \times 10^4$ cm/s. Notably, the y-intercept of the fitted line also directly indicates the asymptotic value of $\tau_{effective}$ where $\tau_{effective}$ approaches $\tau_{surface}$ as d approaches infinity.

DOI: 10.1021/acs.nanolett.7b01770
Nano Lett. 2017, 17, 5356−5360

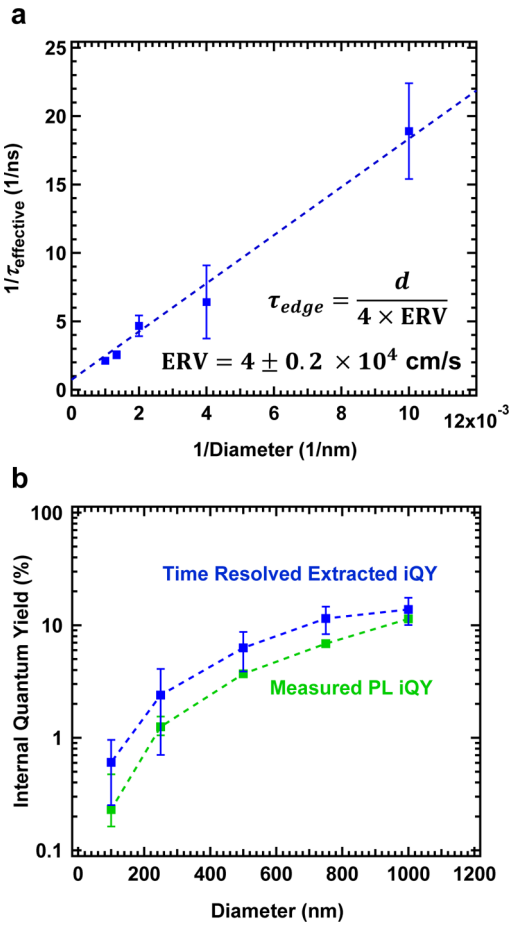

Figure 4. (a) Reciprocal of effective lifetime measured by TRPL versus reciprocal of diameter. Error bars signify the standard deviation of multiple samples of the same designed diameter. (b) Extracted internal quantum yield from both steady-state PL (green) and TRPL (blue) measurements. Error bars on the steady-state PL iQY curve represent absorption error.

It is important to compare the steady-state PL iQY in Figure 2b against the lifetime measurements shown in Figure 3 to verify self-consistency between the two experiments. To this end, we directly compare the iQY values extracted from both measurements. For the TRPL data in Figure 3, we find the time-resolved extracted iQY via:

$$\text{iQY} = \frac{\tau_{\text{effective}}}{\tau_{\text{rad}}} \tag{7}$$

Figure 4b shows from the iQY comparison between quantities calculated from measured decay curves of TRPL (blue) and those directly extracted from steady state PL (green) at the low excitation regime. Both sets of iQY values show a similar trend of decay and are in good agreement. The error bars on the PL iQY curve represent the uncertainty in the absorption measurements, while the error bars on time-resolved extracted iQY curve reflect the spread in the extracted $\tau_{\text{effective}}$ mentioned previously.

To understand ERV as a metric of nonradiative edge recombination in 2D semiconductors, we draw attention to a similar metric extensively utilized by the optoelectronics community, called surface recombination velocity (SRV). SRV is used for describing the surface quality of a 3D semiconductor by quantifying the nonradiative carrier recombination sites at the surface and is a key figure of merit for projecting the maximum performance of the enabled optoelectronic devices based on a 3D semiconductor.[11] Generally, SRV can range from high quality passivated silicon surface of <1 cm/s to unpassivated silicon surfaces spamming into the 10^4–10^5 cm/s regimes.[17−19]

Similar to SRV and the critical role it plays in quantifying surface recombination, ERV can also serve as a key figure of merit for nonradiative carrier recombination at the edge of 2D materials. To see this, we define ERV as

$$\text{ERV} = (N_t/l)\sigma_{1D}\upsilon_{\text{th}} \tag{8}$$

where N_t/l is a linear density of nonradiative recombination sites along a defined perimeter, σ_{1D} is the atomic capture radius of diffusing excitons, and υ_{th} is the thermal velocity of excitons. Equation 8 follows from the general lifetime expression:

$$\frac{1}{\tau_{\text{edge}}} = \frac{N_t}{A}\sigma_{1D}\upsilon_{\text{th}} \tag{9}$$

and making the appropriate substitution from eq 6 where N_t/A is the areal density of nonradiative recombination sites.

Equation 8 allows us to calculate the density of nonradiative recombination sites at a 2D material edge. To illustrate this, we approximate the nonradiative edge recombination sites density N_t/l on our measured WS_2 system using a capture radius on the order of the atomic radius $\sigma_{1D} \sim 10^{-8}$ cm and an exciton thermal velocity $\upsilon_{\text{th}} \sim 10^5$ cm/s.[20,21] The υ_{th} value is estimated using experimentally measured diffusion length of excitons in transition metal dichalcogenides (10^{-4}–10^{-5} cm) divided by the measured lifetime (~1·ns).[22,23] The value used also falls within the range of reported exciton υ_{th} from inorganic materials such as GaAs/AlGaAs quantum wells and thin silicon (10^6 to 10^7 cm/s) to organic molecules such as anthracene (10^4 cm/s).[24−27] With our measured ERV, we calculate $N_t/l \approx 4.4 \times 10^7$ cm^{-1}, corresponding to a nonradiative recombination site per ~2 Å edge length. The estimated density hints at nonradiative recombination at nearly every edge atom, underlying the need for better passivation schemes in the future. This is expected given that certain edge orientations are calculated to exhibit metallic behavior.[13]

In summary, a simple direct optical characterization method enables the experimental measurement of ERV, a quantitative metric directly related to the optical quality of the edge of 2D materials. Using WS_2 as a model material system, we measure ERV of 4×10^4 cm/s for Cl-plasma etched edges. The approach can be extended to other optically active 2D semiconductors. In the future, ERV can be used as an edge quality metric to explore the effectiveness of different edge passivation schemes.

■ ASSOCIATED CONTENT

Supporting Information

The Supporting Information is available free of charge on the ACS Publications website at DOI: 10.1021/acs.nanolett.7b01770.

Optical measurement details, laser spot size calibration, absorption measurements, additional lifetime data, PMMA A2 effects, chlorine plasma etching results, detailed fabrication methods, and τ_{edge} derivation via the diffusion equation (PDF)

DOI: 10.1021/acs.nanolett.7b01770
Nano Lett. 2017, 17, 5356−5360

AUTHOR INFORMATION

Corresponding Author

*E-mail: ajavey@eecs.berkeley.edu.

ORCID

Der-Hsien Lien: 0000-0001-6774-2074
Joel W. Ager III: 0000-0001-9334-9751
Ali Javey: 0000-0001-7214-7931

Notes

The authors declare no competing financial interest.

ACKNOWLEDGMENTS

Nanofabrication and processing of monolayers were supported by NSF E3S Center. PL, TRPL, and absorption measurements were supported by the Electronic Materials Program, funded by Director, Office of Science, Office of Basic Energy Sciences, Materials Sciences and Engineering Division of the U.S. Department of Energy under contract no. DE-AC02-05Ch11231.

ABBREVIATIONS

2D, two dimension
iQY, internal quantum yield
PMMA, poly(methyl methacrylate)
PL, photoluminescence
PL iQY, photoluminescence internal quantum yield
TRPL, time-resolved photoluminescence
SRV, surface recombination velocity
ERV, edge recombination velocity

REFERENCES

(1) Fang, H.; Chuang, S.; Chang, T. C.; Takei, K.; Takahashi, T.; Javey, A. *Nano Lett.* **2012**, *12* (7), 3788−3792.
(2) Li, D.; Cheng, R.; Zhou, H.; Wang, C.; Yin, A.; Chen, Y.; Weiss, N. O.; Huang, Y.; Duan, X. *Nat. Commun.* **2015**, *6*, 7509.
(3) Radisavljevic, B.; Radenovic, A.; Brivio, J.; Giacometti, V.; Kis, A. *Nat. Nanotechnol.* **2011**, *6* (3), 147−150.
(4) Ross, J. S.; Klement, P.; Jones, A. M.; Ghimire, N. J.; Yan, J.; Mandrus, D. G.; Taniguchi, T.; Watanabe, K.; Kitamura, K.; Yao, W.; Cobden, D. H.; Xu, X. *Nat. Nanotechnol.* **2014**, *9* (4), 268−272.
(5) Sundaram, R. S.; Engel, M.; Lombardo, A.; Krupke, R.; Ferrari, A. C.; Avouris, P.; Steiner, M. *Nano Lett.* **2013**, *13* (4), 1416−1421.
(6) Tosun, M.; Chuang, S.; Fang, H.; Sachid, A. B.; Hettick, M.; Lin, Y.; Zeng, Y.; Javey, A. *ACS Nano* **2014**, *8* (5), 4948−4953.
(7) Desai, S. B.; Madhvapathy, S. R.; Sachid, A. B.; Llinas, J. P.; Wang, Q.; Ahn, G. H.; Pitner, G.; Kim, M. J.; Bokor, J.; Hu, C.; Wong, H.-S. P.; Javey, A. *Science* **2016**, *354* (6308), 99−102.
(8) Amani, M.; Lien, D.-H.; Kiriya, D.; Xiao, J.; Azcatl, A.; Noh, J.; Madhvapathy, S. R.; Addou, R.; Kc, S.; Dubey, M.; Cho, K.; Wallace, R. M.; Lee, S.-C.; He, J.-H.; Ager, J. W.; Zhang, X.; Yablonovitch, E.; Javey, A. *Science* **2015**, *350* (6264), 1065.
(9) Amani, M.; Burke, R. A.; Ji, X.; Zhao, P.; Lien, D.-H.; Taheri, P.; Ahn, G. H.; Kirya, D.; Ager, J. W.; Yablonovitch, E.; Kong, J.; Dubey, M.; Javey, A. *ACS Nano* **2016**, *10* (7), 6535−6541.
(10) Amani, M.; Taheri, P.; Addou, R.; Ahn, G. H.; Kiriya, D.; Lien, D.-H.; Ager, J. W.; Wallace, R. M.; Javey, A. *Nano Lett.* **2016**, *16* (4), 2786−2791.
(11) Shockley, W. *Electrons and Holes in Semiconductors with Applications to Transistor Electronics*; D. Van Nostrand Company, Inc: Princeton: New York, 1950; p 576.
(12) Lin, T.; Kang, B.; Jeon, M.; Huffman, C.; Jeon, J.; Lee, S.; Han, W.; Lee, J.; Lee, S.; Yeom, G.; Kim, K. *ACS Appl. Mater. Interfaces* **2015**, *7* (29), 15892−15897.
(13) Huo, N.; Li, Y.; Kang, J.; Li, R.; Xia, Q.; Li, J. *Appl. Phys. Lett.* **2014**, *104* (20), 202406.
(14) Tongay, S.; Suh, J.; Ataca, C.; Fan, W.; Luce, A.; Kang, J. S.; Liu, J.; Ko, C.; Raghunathanan, R.; Zhou, J.; Ogletree, F.; Li, J.; Grossman, J. C.; Wu, J. *Sci. Rep.* **2013**, *3*, 2657.
(15) Ivan Pelant, J. V. *Luminescence Spectroscopy of Semiconductors*; Oxford University Press: New York, 2012; p 542.
(16) Preus, S. *DecayFit - Fluorescence Decay Analysis Software*, 1.4; FluorTools, 2014.
(17) Wolford, D. J.; Gilliland, G. D.; Kuech, T. F.; Smith, L. M.; Martinsen, J.; Bradley, J. A.; Tsang, C. F.; Venkatasubramanian, R.; Ghandi, S. K.; Hjalmarson, H. P. *J. Vac. Sci. Technol., B: Microelectron. Process. Phenom.* **1991**, *9* (4), 2369−2376.
(18) Baek, D.; Rouvimov, S.; Kim, B.; Jo, T.-C.; Schroder, D. K. *Appl. Phys. Lett.* **2005**, *86* (11), 112110.
(19) Yablonovitch, E.; Allara, D. L.; Chang, C. C.; Gmitter, T.; Bright, T. B. *Phys. Rev. Lett.* **1986**, *57* (2), 249−252.
(20) Nakamura, M.; Suzuki, T.; Fujita, M. *Phys. Rev. B: Condens. Matter Mater. Phys.* **1987**, *35* (6), 2854−2862.
(21) Schramm, G. *Phys. Status Solidi A* **1991**, *125* (2), K113−K116.
(22) Kato, T.; Kaneko, T. *ACS Nano* **2016**, *10* (10), 9687−9694.
(23) Kumar, N.; He, J.; He, D.; Wang, Y.; Zhao, H. *J. Appl. Phys.* **2013**, *113* (13), 133702.
(24) Harris, C. I.; Monemar, B.; Holtz, Ro.; Kalt, H.; Mert, J. L. *J. Phys. IV* **1993**, *03* (C5), 171−174.
(25) Tamor, M. A.; Wolfe, J. P. *Phys. Rev. Lett.* **1980**, *44* (25), 1703−1706.
(26) Avakian, P.; Merrifield, R. E. *Mol. Cryst.* **1968**, *5* (1), 37−77.
(27) Levinson, J.; Weisz, S. Z.; Cobas, A.; Rolón, A. *J. Chem. Phys.* **1970**, *52* (5), 2794−2795.

DOI: 10.1021/acs.nanolett.7b01770
Nano Lett. 2017, 17, 5356−5360

Supporting Information

Measuring Edge Recombination Velocity of Monolayer Semiconductors

Peida Zhao[1,3], Matin Amani[1,3], Der-Hsien Lien[1,3], Geun Ho Ahn[1,3], Daisuke Kiriya[1,3], James P. Mastandrea[2,3], Joel W. Ager III[2,3], Eli Yablonovitch[1,3], Daryl Chrzan[2,3], and Ali Javey[1,3,]*

[1] Electrical Engineering and Computer Sciences, University of California at Berkeley, Berkeley, California 94720, United States

[2] Materials Science and Engineering, University of California at Berkeley, Berkeley, California 94720, United States

[3] Materials Sciences Division, Lawrence Berkeley National Laboratory, Berkeley, California 94720, United States

[*]Corresponding Author: ajavey@eecs.berkeley.edu

S1. Optical Characterization Methods

All optical experimental setups utilized for photoluminescence (PL), time-resolved photoluminescence (TRPL), and absorption measurements are performed on a home built system described in detailed elsewhere, including methods used to perform calibrated PL measurements to determine internal quantum yield.[1] Due to the small disk diameters used in this study, several critical aspects of the measurement are described in further details below.

S1.1 Spot size calibration

Laser spot size for this experiment is of particular importance due to our disk sizes, and the fabricated single disk (or array) structures have all been designed to accommodate for this factor.

We measured the beam shape in our micro-PL system by taking an image of the beam using our optical microscope. A profile of the beam intensity is shown in Fig. S1 a, and can be fit using a Gaussian distribution with a standard deviation of +/- 0.7 μm. All single disk sizes fall within +/- 1 standard deviation from the mean (1.4 μm). Fig. S1 b shows the variation in intensity due to the beam's Gaussian nature as a function of disk size. We see that the excitation peak intensity variation yields ~30% difference between the largest (1 μm) and smallest (250 nm) single disk structures. We utilize the Gaussian beam distribution to calculate the incident laser power on the sample.

To accommodate for the measured beam spot size, single disks from 1 μm to 250 nm in diameter are fabricated in the middle of an 8 μm x 8 μm field (whose field size is chosen to give comfortable tolerance to both stage drifts and accommodate the

measured beam spot size), where the exposed regions are subsequently etched away, leaving only the desired WS_2 monolayer disk at the field center. The field clearance allows the optical setup to only collect the luminescence contribution from the monolayer disk itself, and not from nearby unetched WS_2. For disk diameters of 100 nm, a disk array is fabricated across an 8 μm x 8 μm field with a center to center disk spacing of 200 nm. The array is designed to maximize signal to noise ratio due to low iQY of the 100 nm disks.

Lastly, special care is also taken during measurement to ensure that the single disk rests directly under the peak excitation intensity. To verify this, each spectra of the single disk sample is taken multiple times as the stage is shifted in all 4 planar directions. This is repeated until the photoluminescence signal is maximized, where we assume that the peak of the laser intensity is exciting the sample disk.

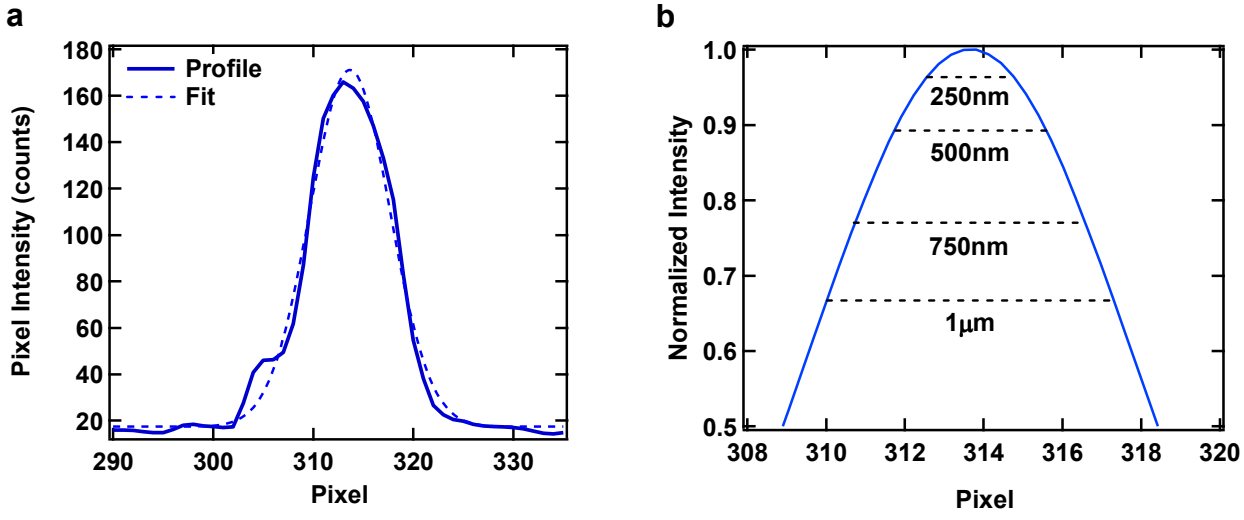

Fig. S1: Laser spot size calibration. (a) Intensity profile of the laser spot size measured in the micro-PL microscope camera. A ~123 nm/pixel scale is determined using a calibrated length standard. A standard Gaussian distribution is to fit the profile with a

single standard deviation 0.7 μm in length. (b) Comparison of disk size with that of the beam shape. The Gaussian beam shape yields a ~30% difference in the peak intensity between the largest (1 μm) and the smallest (250 nm) single disk size samples.

S1.2. **Absorption Measurements**

Due to the subwavelength nature of the disk diameters (compared to the 514nm excitation wavelength), it is important to experimentally measure absorption for the smaller disk sizes. WS_2 disk arrays of 500 nm, 250 nm, and 100 nm were fabricated on quartz for absorption measurements. Specifically, repeating disks of a chosen diameter is patterned across an 8 μm x 8 μm field (with a center to center spacing of 2*d*). The samples are mounted in a transmission microscope, allowing for measurement of the reflected and transmitted laser power in the sample and on a blank quartz substrate. Fig. S2 shows the absorption calculated from the reflection and transmission results for all three array sizes. Due to the array structure utilized in all three sizes, the measured absorption incorporates both the intrinsic absorption change and the array fill factor. A constant fill factor of ~20% is calculated given the center to center spacing, and the intrinsic absorption is then extracted. The results here allow us to calculate both the generation rate and PL iQY of the smaller disk samples at the subwavelength regime.

It is important to note that due to its low absorption value the 100 nm diameter sample shows significant measurement variation. This is directly reflected by the error bars in Figure 2b.

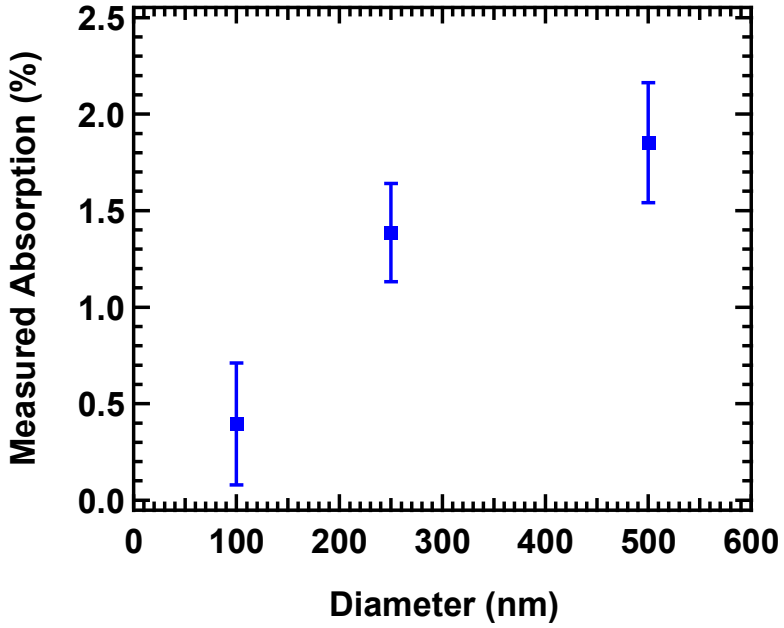

Fig. S2: Absorption Measurements of disks with $d \geq 500$ nm. A disk array is utilized for all three sizes in order to maximize signal to noise ratio. The absorption is derived by a one beam transmission/reflection setup where the signal is collected by a photodetector and read by a lock-in amplifier. The error bars represent uncertainty of multiple reflection and transmission measurements.

S1.3 τ_{edge} and $\tau_{effective}$ vs. Disk Diameter

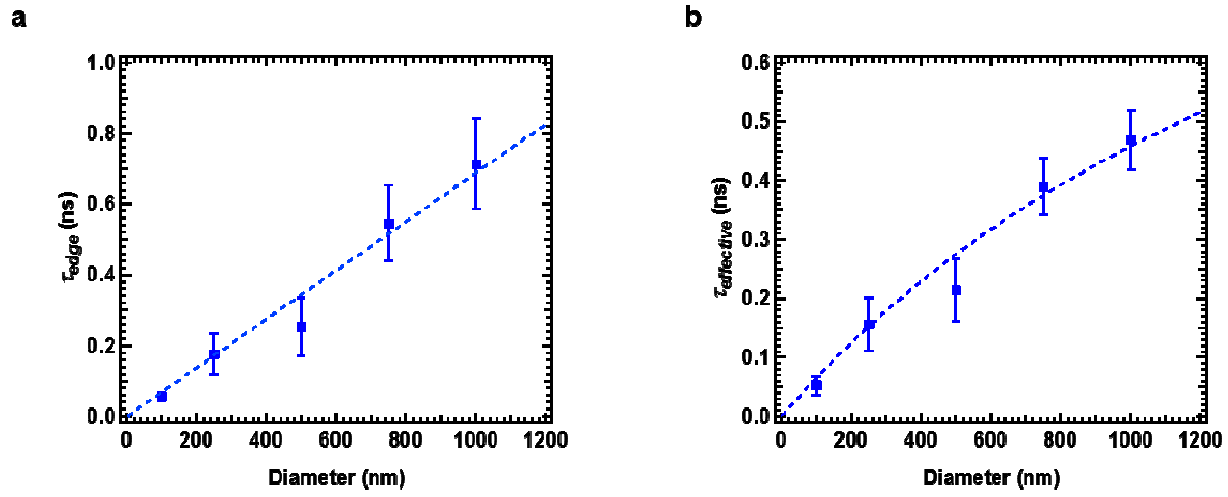

Fig. S3: The specific τ_{edge} and $\tau_{effective}$ vs. *d* behaviors are presented here. Fig. S3a shows the extracted τ_{edge} vs. *d*, displaying an expected linear relation and facilitating a clear fit whose slope is $(4 \times \mathrm{ERV})^{-1}$. Fig. S3b shows an asymptotically flattening $\tau_{effective}$ vs. *d* curve with the effective lifetime approaching that of $\tau_{surface}$ described in the main text. The error bars represent the standard deviation of all measured samples with the same designed *d*.

S1.4 Etching and Passivation Methods Explored, and Their Impacts on ERV

The monolayer edges investigated in this work are etched by chlorine plasma. The ERV is expected to depend on the etching method as well as the 2D material itself. To further understand the impact of etching methods on ERV, we also attempted WS_2 monolayer etching using argon plasma, fluorine based (SF_6, CF_4) plasma, and XeF_2 isotropic gas etch. Out of the four methods, argon plasma did not effectively remove the monolayer within the used energy range. Fluorine plasma and XeF_2 etched the monolayers effectively, though the latter had undercutting issues.

For monolayer disks of the same diameters, the two fluorine based etching methods (SF_4 and CF_4) result in similar PL intensity. Additionally, the PL intensity of monolayer disks patterned by chlorine and fluorine plasma etching is similar within an order of magnitude. Figure S4 demonstrates the PL intensity of WS_2 disk arrays etched by chlorine and fluorine based plasma.

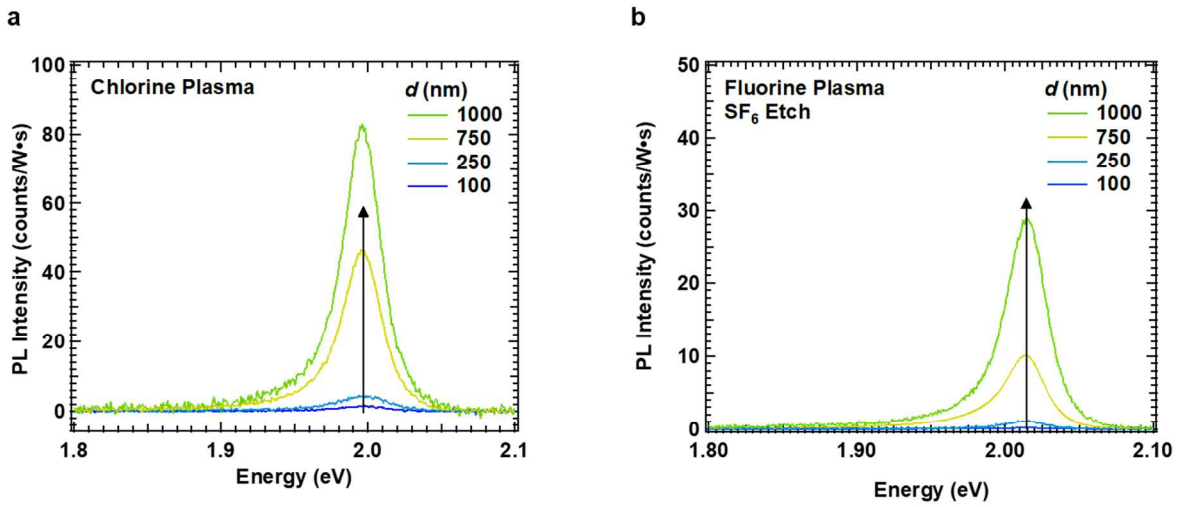

Fig. S4: PL spectra of disk arrays etched via (a) chlorine and (b) fluorine based plasma. The peak intensity differences between the two etching methods vary by 2-4x, and is mostly attributed to experimental variations.

Additionally, we investigated potential passivation methods aimed to improve ERV after the initial plasma etching. A short table (Table S1) is included below describing both the treatment methods and the change in PL intensity of 100 nm WS_2 disk arrays after plasma dry etch:

Wet Treatments	**PL Peak Intensity Change in 100nm WS_2 Disk Arrays**
Bis (trifluoromethane) sulfonimide (TFSI) Solvent: Dichloroethane (2mg/ml)	~ 2-3x enhancement
Triethyloxonium Hexachloroantimonate: Solvent: Chlorobenzene (0.1M)	< 2x change
Sulfuric Acid (1M)	< 2x change
Hydrochloric Acid (>1M)	< 2x change
Hydrofluoric Acid (10:1)	~ 3x reduction and observed defect peak
Ammonium Sulfide (20% in water) Solvent: H_2O (0.2g/15ml)	~ 2x reduction
Gas Annealing	
Forming Gas (300 ^oC)	< 2x reduction and large peak broadening

O_2 Plasma (40W for 5 seconds)	< 2x reduction
Ambient Oxygen Anneal (250 ^oC)	< 2x change
Physical Depositions	
Al_2O_3 (70 cycles at 250 ^oC) – ALD	< 2x change
ZrO_3 (70 cycles at 200 ^oC) – ALD	>3x reduction
SiO_2 (10nm) – eBeam Evaporation	< 2x change
WO_3 (2 cycles at 350 ^oC) – ALD	~ 2x reduction and large peak broadening

Table S1: Various techniques used to improve the PL intensity of the 100 nm array samples. No significant improvement of the PL intensity can be seen across different treatments.

The lack of significant PL intensity improvement after various treatments is interesting and perplexing. We postulate, from reactive ion etching theory and our own AFM data, that an inhibitor layer forms at the edges after the etching process. These inhibitor walls render any subsequent treatments ineffective, as they are difficult to remove or replace. Further studies are needed to completely understand the edge chemistry, and develop new etching processes to overcome the current limitations of plasma etching in the monolayer system.

S2. Fabrication

S2.1. Sample Preparation and Lithography

All flakes used in this work were exfoliated from a WS_2 source (HQ Graphene). After tape exfoliation on a quartz substrate, the samples were patterned with electron beam lithography with poly methyl methacrylate (PMMA A2) (3000 rpm at 30 seconds, yielding a thickness at ~50-60 nm) as the resist and a 7-8 nm thermally evaporated gold

film as the conduction layer. After a short gold etch in potassium iodide and development in a diluted methyl isobutyl ketone solution (in 1:3 isopropanol), the samples were etched in a local transformer coupled plasma tool in the presence of 30 sccm chlorine gas for 22 seconds at 40 W power. The resist was then removed in a 2-hour hot acetone bath, followed by various optical characterizations. Forming gas (5% nitrogen balance at 350°C for 2 hours) is used for carbon residue cleaning.

We verify both PMMA's effects on the WS_2 emission as the monolayer undergoes fabrication, and also the effectiveness of the PMMA as a soft etch mask. Fig. S5a shows the photoluminescence spectra of a WS_2 flake both before and after a layer of PMMA A2 is spun coat on top at the same condition used for patterning disks. We observe no obvious difference in the emission and conclude that PMMA itself does not affect (or degrade) WS_2 emission properties in any significant way. Fig. S5b shows the photoluminescence spectra of a WS_2 flake before and after the standard dry etch step used to define disks with the entire flake covered by PMMA A2. No significant change to the PL spectra is observed with the protective PMMA layer resting on top of the WS_2.

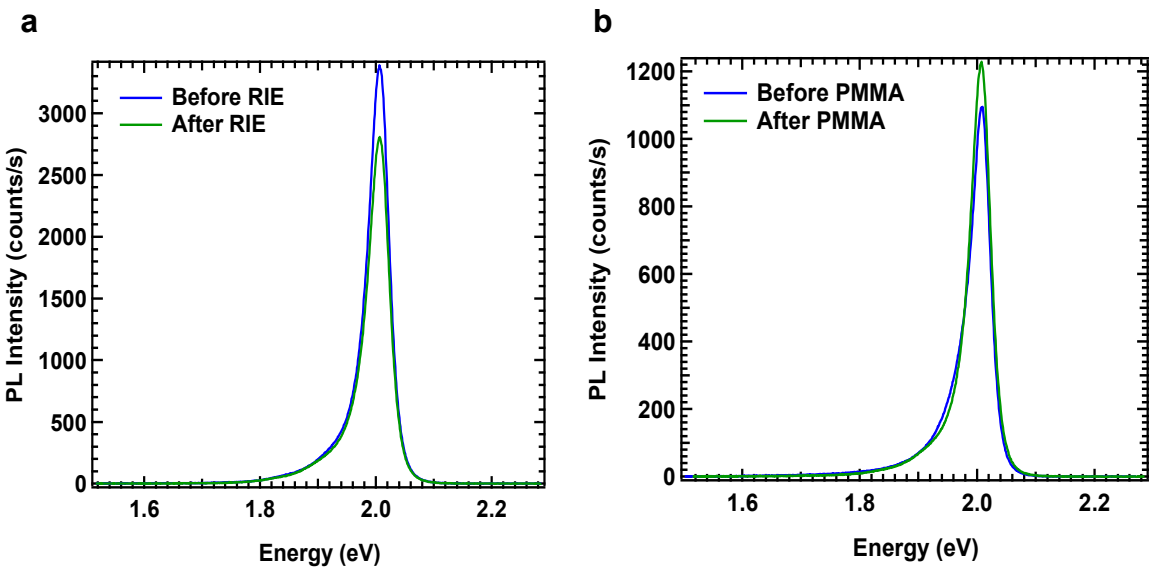

Fig. S5: Effects of PMMA A2 on monolayer WS_2 emission, and effectiveness of PMMA A2 as a soft mask for chlorine etching. (a). PL spectra shows no effective change on monolayer WS_2 emission before and after PMMA spin-coating. (b) PL spectra also shows no effect on WS_2 emission after the standard etch step when the entire flake is protected by the PMMA.

S2.2 Chlorine Plasma Etching Optimization

The dry etching technique used here is taken from a previously reported layer-by-layer etching technique.[2] Due to equipment constraints, however, only Cl_2 is used here as an etchant gas. Therefore, control tests were performed to verify successful etching.

At a much harsher condition, the Cl plasma dry etch demonstrates clear capability of removing thick WS_2 without leaving any significant residue as seen via atomic force microscope, as shown in Fig. S6a. Utilizing a milder condition etch single layers, a clear change in the etch rate is observed, where approximately a monolayer

can be etched away. This is substantiated via both the color contrast and AFM scan (Fig. S6b).

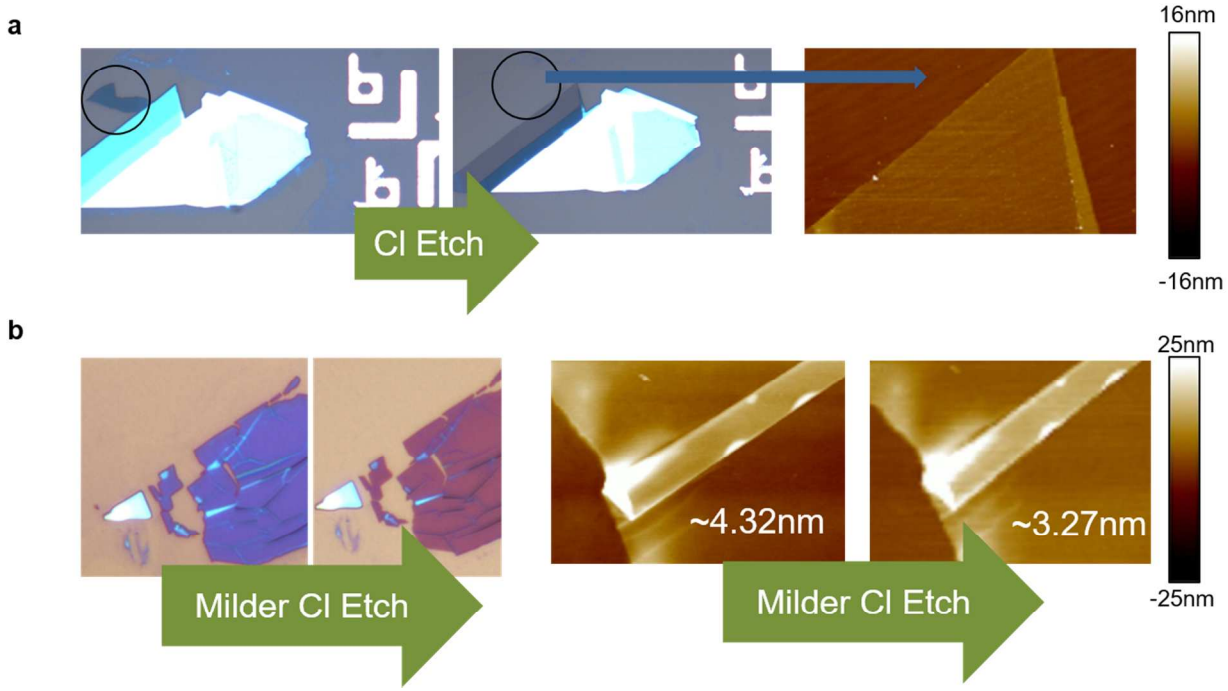

Fig. S6: Chlorine dry etch results, with both harsh and mild conditions. (a) At the harsher conditions, we observe a very clean etch of the protruding blue section of the flake circled in the illustration. We also verified under AFM to ensure that the flake is indeed etched and that negligible to no residues are present. (b) At the milder Cl etching conditions, we observe layer-by-layer etching that is used to pattern WS_2 disks and yields no visible residue or damage under the AFM.

S2.3 AFM Thickness

Here we present the topology data of each sample shown in Figure 1c. Each sample flake has approximately 1nm in step height, representative of a monolayer

thickness. Variation in the topology comes from the roughness of the quartz substrate used and processing.

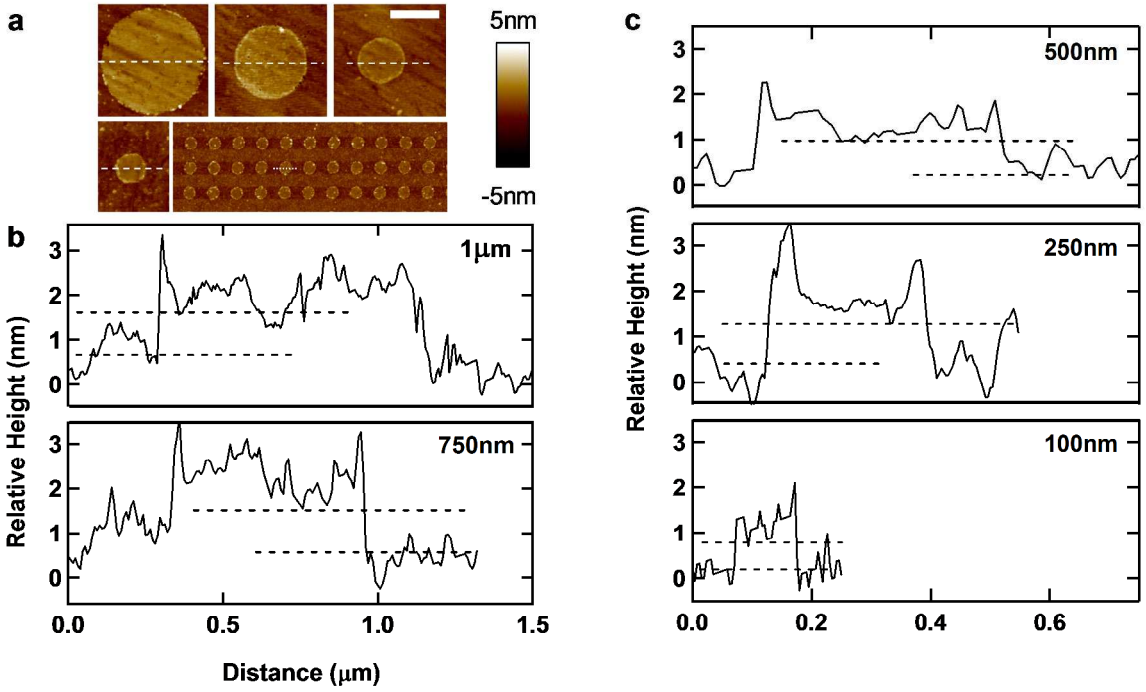

Fig. S7: (a). Replicated graph of Fig. 1c showing exactly where the thickness topologies of the subsequent panels are taken from. (b). Thickness graph of 1 um and 750 nm thick WS_2 disks. (c). Thickness graph of 500 nm, 250 nm, and 100 nm thick 100 WS_2 disks. The dash lines are a guide for the eye in comparison with the vertical axis, they're representative of ~1 nm in spacing.

S3. ERV Derivation *via* Diffusion Equation

Starting with existing diffusion models[3], we provide here a detailed derivation of the edge recombination velocity expression:

$$\tau_{\text{edge}} = \frac{d}{4 \times \text{ERV}} \tag{S.1}$$

We assume that the carriers are governed by diffusive dynamics, with the diffusion coefficient D independent of the carrier concentration.

We also express distance in units of $d/2$, with d being the disk diameter. Time (and the relaxation time) is measured in units of $d^2/4D$. With these units, the dimensionless diffusion equation becomes (assuming cylindrical symmetry):

$$\frac{\delta C}{\delta t} = \frac{1}{r}\frac{\delta}{\delta r}\left(rD\,\frac{\delta C}{\delta r}\right) - \frac{C}{\tau} \tag{S.2}$$

With $C(r,t)$ being the carrier concentration, r the dimensionless radius, and τ the dimensionless relaxation time. The edge induced recombination rate is represented as a flux of carriers at the edge of the disk. In dimensionless form, this boundary condition is given by:

$$-D\,\frac{\delta C}{\delta r}\Big|_{r=1} = \alpha C|_{r=1} \tag{S.3}$$

With $\alpha = d/2D \times \text{ERV}$,the dimensionless recombination velocity. The solution to this equation can be constructed in the form of a Dini series. Assuming that the initial condition is a uniform concentration of carriers, C_o, the solution is given by:

$$C(r,t) = C_o \sum_{n=1}^{\infty} \frac{2\alpha}{(k_m^2 + \alpha^2)} \frac{J_0(k_m r)}{J_0(k_m)} \exp\left[-\left(k_m^2 + 1/\tau\right)t\right] \tag{S.4}$$

With $J_v(x)$ being the Bessel function of the order v and k_m being the mth root of:

$$k_m J_1(k_m) = \alpha J_0(k_m) \tag{S.5}$$

This expression then, gives the complete solution to our problem.

The total light emitted at dimensionless time t is proportional to the total number of carriers:

$$\text{intensity} \propto \frac{2\pi}{\tau_{\text{rad}}} \int_0^1 dr\, r\, C(r,t) \tag{S.6}$$

With τ_{rad} being the relaxation time for radiative recombination. In the long-time limit, the intensity becomes proportional to:

$$\text{intensity} \propto \exp\left[-\left(k_1^2 + {}^1\!/_{\tau}\right)t\right] \tag{S.7}$$

The total dimensionless relaxation time becomes $(k_1^2 + {}^1\!/_{\tau})^{-1}$, with the corresponding edge relaxation time becoming k_1^2. Restoring dimensions, we find that

$$\tau_{\text{edge}} = \frac{d}{4D} k_1^{-2} \tag{S.8}$$

For small α, the solution to (S.5) for $k_1$can be approximated as $k_1 = \sqrt{2\alpha}$.[4] Substituting this expression into (S.8) and noting that $\alpha = {}^d\!/_{2D} \times \text{ERV}$, we find:

$$\tau_{\text{edge}} = \frac{d}{4D} k_1^{-2} = \frac{d}{4D} \frac{1}{2\alpha} = \frac{d}{4 \times \text{ERV}} \tag{S.9}$$

As noted in the main text.

The quality of the $k_1 = \sqrt{2\alpha}$ approximation can be assessed via Fig. S6 that plots both the exact solution for k_1 and its approximate expression for $0 < \alpha < 1$.

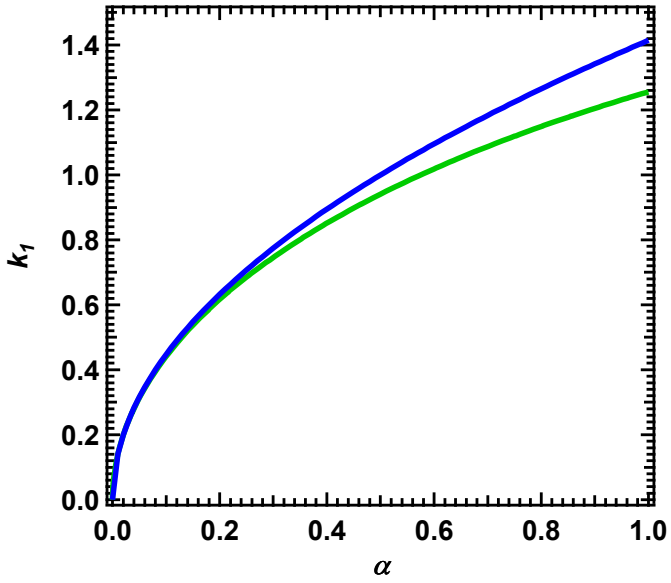

Fig. S6: Graphical comparison for both the exact solution to (S.5) for k_1 (blue curve) and the approximation $k_1 = \sqrt{2\alpha}$ (black curve). The error at $\alpha = 1$ is approximately 13%.

Supplementary References

(1) Amani, M.; Lien, D.-H.; Kiriya, D.; Xiao, J.; Azcatl, A.; Noh, J.; Madhvapathy, S. R.; Addou, R.; Kc, S.; Dubey, M.; Cho, K.; Wallace, R. M.; Lee, S.-C.; He, J.-H.; Ager, J. W.; Zhang, X.; Yablonovitch, E.; Javey, A. *Science* **2015**, 350, (6264), 1065.

(2) Lin, T.; Kang, B.; Jeon, M.; Huffman, C.; Jeon, J.; Lee, S.; Han, W.; Lee, J.; Lee, S.; Yeom, G.; Kim, K. *ACS Appl. Mater. Interfaces* **2015**, 7, 15892-15897.

(3) J. Crank, *The Mathematics of Diffusion.* Clarendon Press: Oxford, 1975; p 79.

(4) Dan, Y.; Seo, K.; Takei, K.; Meza, J. H.; Javey, A.; Crozier, K. B. *Nano Lett.* **2011**, 11, (6), 2527-2532.